

MOUNTAIN-PLAINS CONSORTIUM

MPC 19-409 | Y. J. Kim

Innovative Strengthening
for Deteriorated Concrete
Bridges Using Embedded
Composite Sheets Bonded
with Polyester-Silica



A University Transportation Center sponsored by the U.S. Department of Transportation serving the Mountain-Plains Region. Consortium members:

Colorado State University
North Dakota State University
South Dakota State University

University of Colorado Denver
University of Denver
University of Utah

Utah State University
University of Wyoming

**Innovative Strengthening for Deteriorated Concrete Bridges
Using Embedded Composite Sheets Bonded with Polyester-Silica**

Yail Jimmy Kim, Ph.D., P.Eng., FACI
Department of Civil Engineering
University of Colorado Denver
Denver, Colorado

December 2019

Acknowledgments

The Principal Investigator gratefully acknowledges all individuals who contributed to the present research report.

Disclaimer

The contents of this report reflect the work of the author, who is responsible for the facts and the accuracy of the information presented. This document is disseminated under the sponsorship of the Mountain-Plains Consortium in the interest of information exchange. The U.S. Government assumes no liability for the contents or use thereof.

NDSU does not discriminate in its programs and activities on the basis of age, color, gender expression/identity, genetic information, marital status, national origin, participation in lawful off-campus activity, physical or mental disability, pregnancy, public assistance status, race, religion, sex, sexual orientation, spousal relationship to current employee, or veteran status, as applicable. Direct inquiries to: Vice Provost, Title IX/ADA Coordinator, Old Main 201, 701-231-7708, ndsuetiaa@ndsu.edu.

EXECUTIVE SUMMARY

This report presents the feasibility of a novel anchor system that mitigates the end-peeling of carbon fiber reinforced polymer (CFRP) sheets used for strengthening reinforced concrete beams. Contrary to conventional anchoring methods, CFRP sheets are embedded inside the pre-grooved concrete and covered by a durable polyester-silica composite. After conducting ancillary tests on material, bond, and interfacial properties, 14 strengthened beams are loaded in flexure to assess the performance of the proposed anchor system, contingent upon embedment angle and local debonding along the bond-line. The polyester-silica matrix shows superior moisture-resistance to ordinary cementitious mortar and possesses a fully-cured compressive strength of 38 MPa as well as interfacial capacities comparable to those of an epoxy adhesive. The embedment angle and local debonding of CFRP affect the flexural behavior of the strengthened beams, including sectional rotation and stress distributions. The presence of mechanical fasteners with supplementary epoxy layers in the anchorage substantially enhances the flexural capacity, energy dissipation, and ductility of the beams. Correlation and sensitivity analyses are performed to analytically characterize the load-carrying capacities of the strengthened beams with variable embedment angles and the degree of local debonding.

TABLE OF CONTENTS

1. INTRODUCTION.....	1
2. RESEARCH SIGNIFICANCE.....	2
3. EXPERIMENTAL PROCEDURE.....	3
3.1 Materials	3
3.2 Ancillary Tests.....	3
3.2.1 Strength of Polyester-silica	3
3.2.2 Porosity of Polyester-silica	3
3.2.3 Bond with Concrete Substrate.....	4
3.2.4 Interface with CFRP.....	4
3.3 Beam Details.....	5
3.3.1 Preparation	5
3.3.2 Strengthening Schemes	5
3.3.3 Loading and Instrumentation	6
4. TEST RESULTS.....	7
4.1 Ancillary Tests.....	7
4.1.1 Porosity of Polyester-silica	7
4.1.2 Strength of Polyester-silica	7
4.1.3 Bond Against Concrete	7
4.1.4 Behavior of Interface.....	7
4.2 Beam Tests.....	8
4.2.1 Load-carrying Capacity.....	8
4.2.2 Failure Mode	8
4.2.3 Flexural Behavior.....	9
4.2.4 Energy Dissipation.....	9
4.2.5 Ductility Assessment.....	10
4.2.6 CFRP Strain	11
5. RESPONSE CHARACTERIZATION	12
5.1 Correlation	12
5.2 Sensitivity	12
6. SUMMARY AND CONCLUSIONS	13
7. REFERENCES.....	14

LIST OF TABLES

Table 1	Test beams	16
----------------	------------------	----

LIST OF FIGURES

Figure 1	Ancillary Tests	17
Figure 2	Beam details	18
Figure 3	Porosity test	19
Figure 4	Material test	19
Figure 5	Interface test	20
Figure 6	Comparison of flexural capacity	20
Figure 7	Failure mode	21
Figure 8	Load-displacement behavior	21
Figure 9	Sectional rotation at midspan	22
Figure 10	Flexural energy up to initial peak load	22
Figure 11	Ductility.....	22
Figure 12	CFRP strain development	23
Figure 13	CFRP strain profile	24
Figure 14	Characterized response	24

1. INTRODUCTION

Carbon fiber reinforced polymer (CFRP) is an alternative to conventional materials and has been employed for the rehabilitation of existing structures for decades (Hollaway 2010). By adhesively bonding CFRP sheets to the tensile side of a concrete member, several benefits are accomplished: upgraded load-carrying capacity, minimal maintenance activities, favorable life cycle costs, and enhanced safety (ACI 2007; ACI 2017). The physical contact of CFRP to the underlying concrete is a foremost requirement for adequate stress transfer, which dictates the efficacy of such a strengthening system. Consequently, extensive research has been conducted to elucidate the debonding mechanism of CFRP-strengthened beams and numerous bond models were proposed (Smith and Teng 2002). In spite of substantial optimism that the bond will be maintained for the service life of strengthening systems, a number of detrimental factors degrade the performance of CFRP-concrete interface, such as moisture, temperature, and mechanical distress, leading to the intermediate-crack-induced debonding (IC-debonding hereafter) and end-peeling of bonded CFRP sheets. IC-debonding initiates at the places where flexural and shear cracks form, and prompts adverse stress transfer from the concrete substrate to CFRP (Wan et al. 2018). End-peeling occurs at the termination of CFRP because of the concentration of shear and normal stresses (Smith and Teng 2002). Contrary to IC-debonding that disrupts local composite action between the concrete and CFRP, end-peeling causes rapid failure of the strengthening system. In that regard, end-peeling is deemed more critical and should be prevented to warrant the sustainable use of CFRP-strengthening technologies.

The integrity of the CFRP-concrete interface is salient for the strengthening system to function properly. Because premature interfacial failure is of concern, various endeavors have been undertaken to address the problem. From a practical point of view, the following approaches are frequently implemented (Kalfat et al. 2013; ACI 2017): effective strain, U-wraps, and mechanical anchorage. ACI 440.2R-17 (ACI 2017) states that the maximum strain of CFRP should not exceed the prescribed effective strain to avoid IC-debonding. U-wraps may be bonded to confine the longitudinal CFRP sheets in a strengthened member, and the fiber direction of CFRP U-wraps is generally perpendicular to the beam span (Lee and Lopez 2019). Mechanical fasteners in combination with metallic plates can replace U-wraps to better clamp the CFRP system (Zhou et al. 2018). Notwithstanding the effectiveness of these debonding mitigation methods, it is still uncertain whether the performance of CFRP-strengthening systems is preserved over years, particularly when subjected to aggressive environments. The effective strain is based on current material properties that do not consider potential changes, U-wraps may debond owing to the degradation of the adhesive, and the mechanical anchors are corrosive. A fundamentally different concept for anchoring CFRP sheets should, therefore, be necessary.

This paper explores the feasibility of a novel anchor system with an emphasis on impeding end-peeling failure. In contrast to the above-described methods, the proposed anchorage is embedded inside a pre-grooved beam and protected by a durable polyester-silica composite matrix. To substantiate the practicality of the embedded CFRP anchors, an experimental program was conducted at material-, interface- and structure-levels. The primary parameters of the investigation were embedment angle and partial debonding, which are crucial to understand the load-bearing mechanism and failure characteristics of the beams with embedded CFRP.

2. RESEARCH SIGNIFICANCE

The bond within a CFRP-concrete interface is instrumental in enabling the intended functionality of strengthened members. End-peeling concerns arise near the CFRP termination, which brings about an irreversible state of the interface and eventually leads to the failure of the strengthening system. Consequently, the use of adequate anchorage is an important consideration when rehabilitating concrete structures with CFRP sheets. With this in mind, a new anchoring technique is proposed to reduce the risk of end-peeling and stress singularities in CFRP-strengthened beams. Test results demonstrate that the embedded CFRP anchors with a polyester-silica composite can be a substitute for existing debonding-control approaches.

3. EXPERIMENTAL PROCEDURE

A two-phase experimental program is described: i) ancillary tests for material characterization and ii) flexural tests using reinforced concrete beams with embedded CFRP sheets. The performance of polyester-silica is of interest when interfaced with the concrete and CFRP, including anchorage application.

3.1 Materials

The laboratory-mixed concrete had an average 28-day compressive strength of 19 MPa with a standard deviation of 0.7 MPa (specified strength = 20 MPa representing concrete undocumented for a field evaluation, CAN/CSA S6-14, CSA 2014) as per ASTM C39 (ASTM 2015). Standard Grade 60 reinforcing steel bars (No. 3) were employed with a nominal yield strength of 414 MPa and an elastic modulus of 200 GPa. The unidirectional CFRP sheets used for strengthening had a manufacturer-guaranteed strength of 3,800 MPa alongside a tensile modulus of 227 GPa and a rupture strain of 0.0167. Two types of matrix materials were utilized: epoxy and polyester-silica. The resin and hardener of the two-part epoxy were blended at a ratio of 3 to 1 by mass, which resulted in a specified tensile strength of 55 MPa and a modulus of 3 GPa after 7 days of curing. The polyester resin was prompted with a catalyst (ratio of 100 g to 1 g) for chemical reactions to achieve a tensile strength and corresponding modulus of 40 MPa and 3.5 GPa, respectively, with an elongation of 0.014 at failure. Silica sand had the following properties: silicon dioxide amount = 90.3%, average particle size = 0.45 mm, specific gravity = 2.62, and pH = 7.0. The polyester-silica composite was produced as follows. The silica and polyester were prepared with a mass ratio of 80:20 and stirred using a spatula until a homogenous matrix was obtained. According to the manufacturer, the setting time of the polyester was 25 minutes at room temperature (48 hours for complete curing).

3.2 Ancillary Tests

3.2.1 Strength of Polyester-silica

Thirty-six polyester-silica cubes (50 mm in length) were cast to examine the time-dependent compressive strength of the composite matrix. Six cubes were loaded in monotonic compression at a rate of 0.5 mm/min per curing time for up to 14 days (Figure 1(a)).

3.2.2 Porosity of Polyester-silica

Following ASTM C948 (ASTM 2009), the apparent porosity and water absorption (P and A in Equations 1 and 2, respectively) of the polyester-silica composite were measured, as shown in Figure 1(b), and compared against those of typical cementitious mortar (mixed with cement and sand at 1:3 by mass). In so doing, the adequacy of the polyester-silica-based anchorage for CFRP-strengthened beams would be justified in terms of durability. Literature reports that moisture-ingress is one of the critical factors degrading the performance of a CFRP-concrete interface (Pan et al. 2019).

$$P(\%) = (B - C) / (B - A) \times 100 \quad (1)$$

$$A(\%) = (B - C) / C \times 100 \quad (2)$$

where A , B , and C are the water-suspended, saturated surface-dry, and dry weights of the specimen, respectively. A total of 12 cubes (50 mm in length, which is within the required size range of ASTM C948, ASTM 2009) were prepared to monitor the porosity and water absorption of the polyester-silica

composite and ordinary mortar over time (3 cubes for dry weight and 3 cubes for water-suspended and saturated weights for each material). During the property measurement for up to 14 days when the strength of the polyester-silica sufficiently developed (discussions follow), physical changes in the specimens such as damage and spalling were not noticed.

3.2.3 Bond with Concrete Substrate

To evaluate the bond of the polyester-silica and epoxy matrices against concrete substrates, a push-down test was conducted using three concrete blocks (50 mm wide by 75 mm deep by 100 mm long, each) per set, as detailed in Figure 1(c). After roughening the substrates with an electric grinder, the blocks were bonded and cured for 14 days. Afterward, all specimens were loaded at a rate of 0.5 mm/min and failure loads were recorded.

3.2.4 Interface with CFRP

Table 1 summarizes the load-carrying capacity of the test beams. The yield and ultimate loads of the unstrengthened beam (control) were 31.1 kN and 34.2 kN, respectively. An obvious relationship was noticed between the flexural capacity and CFRP-embedment angle in Phase I. The B100-25-PS beam (25 degrees) failed at a load of 58.1 kN, which was 11.5% higher than the B100-0-PS beam (0 degrees). The trend of the consistently increasing capacity with the embedment angle is graphed in Figure 6(a). Since the embedment angle of 25 degrees resulted in the most favorable capacity, it was adopted in Phases II and III.

The implications of local debonding, represented by the partially bonded CFRP sheets, were apparent (Figure 6(b)). The full-bond beam (100%) exhibited an increase of 69.9% in the ultimate load compared with the control beam. Unlike the variation of the yield load in the 80%- and 60%-bond beams, their ultimate loads were maintained. This fact illustrates that the occurrence of local debonding reduced the degree of stress-shearing between the internal and external reinforcements (steel and CFRP, respectively), thereby increasing the steel strains; however, the extent of CFRP-debonding was insufficient to influence the overall capacity of the beams (further discussions are available in the subsequent section). As the bond length decreased below 40%, noticeable capacity drops were recorded, which are ascribed to a dearth of the interaction between the beam and CFRP.

On the efficacy of epoxy-bonding in Phase III, the presence of the epoxy layer between the concrete substrate and the polyester-silica base precluded disintegration of the anchorage and induced an 8.8% increase in the ultimate load (B100-25-PSE vs. B100-25-PS in Table 1). Additional improvements in the capacity of the strengthened beams were accomplished by the mechanical fasteners; the failure loads of B100-25-PM and B100-25-PME were, respectively, 2.4% and 5.4% higher than that of B100-25-PSE.

A series of interface tests were carried out to confirm the applicability of the proposed embedded anchor system. Concrete blocks (300 mm long by 50 mm wide by 100 mm high) were cast with a groove of 180 mm long by 25 mm deep, as depicted in Figure 1(d). The CFRP-bonding of variable embedment angles was tested from 10 to 25 degrees at 5-degree increments. An inclined base substrate was formed in the cured concrete block using the polyester-silica and epoxy matrices (masking tapes were temporarily utilized for shaping and removed later), and a single layer of precut CFRP sheet (50 mm wide) was placed to envelop the entire groove (Figure 1(d)). Thereafter, the groove was filled with the individual matrices and cured for 14 days. Note that the primary interest of the test rested in the performance of the polyester-silica composite, while the epoxy-bonded specimens rendered comparative information. The interface specimens were mounted in a universal testing machine and tensioned at a rate of 0.5 mm/min until failure.

3.3 Beam Details

3.3.1 Preparation

Concrete beams (100 mm wide by 165 mm deep by 1.4 m long) were reinforced with two No. 3 steel bars (Figure 2(a)). For the convenience of anchorage installation, styrofoam blocks (180 mm long by 25 mm deep by 100 mm wide) were placed near the ends of the beam prior to pouring concrete, and eliminated after curing. The tensile soffit of the beams was prepared by an electric grinder and air-brushed for cleaning.

3.3.2 Strengthening Schemes

Three strengthening phases were tested, contingent upon CFRP embedment angle, bond length, and anchorage configuration, as enumerated in Table 1 with identification codes. For example, B100-10-PS indicates that a strengthened beam had a 100% CFRP-bond length at an embedment angle of 10 degrees in the anchorage with polyester-silica substrates. The objectives of Phase I were to examine the influence of the embedment angle on the behavior of the strengthened beams and to assess their angle-dependent flexural capacity. Phase II was concerned with the effects of local CFRP-debonding (that is, IC-debonding outside the anchorage region) on the capacity and ductility of the beams, based on the angle that would result in the highest ultimate load in Phase I. The emphasis of Phase III was placed on the effectiveness of epoxy bonding and mechanical fasteners when used with the embedded CFRP anchor system.

As in the case of the interface specimens, base substrates were cast for the Phase I beams employing the polyester-silica matrix at an angle varying from 10 to 25 degrees (Figure 2(a)). An epoxy layer was applied along the concrete soffit and inside the grooves over the hardened base substrates, and a single layer of dry carbon fabric (100 mm wide by 1,090 mm long) was impregnated to form CFRP, followed by another topcoat layer of the epoxy. The anchorage regions were then fully filled with the premixed polyester-silica and cured for 14 days (this covering was implemented in all phases). Regarding the Phase II beams, the base substrate was cast at the angle of 25 degrees, which would have provided the most favorable capacity in the Phase I test (to be discussed), and local debonding was represented by partially pasting the epoxy along the concrete substrate: 0% to 100% of the CFRP bond length outside the anchorage zones (Figure 2(a)). The Phase III beams had base substrates at 25 degrees, like the Phase II beams; however, an additional epoxy layer was applied between the base substrates and the concrete surface, and a mechanical fastener system was installed with and without epoxy layers (PS+EP, PS+MF, and PS+MF+EP, as defined in Table 1 and Figure 2(b)). For the B100-25-PM beam, the grooved concrete was drilled to insert two expansion mechanical fasteners per anchorage (Φ 10 mm by 50 mm long) and the CFRP sheet was fully bonded (100% bonding). Note that the carbon fibers were not damaged because the fasteners were positioned in the gaps between the longitudinal fibers before hardening. Stainless steel plates (100 mm by 50 mm, each) with predrilled holes were properly positioned (Figure 2(b)) and the fasteners were pushed in. The application steps of the B100-25-PME beam were identical to those of the B100-25-PM beam, except that the epoxy adhesive was pasted to all interfaces where dissimilar materials were in contact: concrete groove and polyester-silica substrate, drilled concrete holes and fasteners, and steel plate and polyester-silica cover.

3.3.3 Loading and Instrumentation

The individual beams were subjected to four-point bending at a loading rate of 1 mm/min, as shown in Figure 2(c). The applied load and midspan displacement were measured by a load cell and a linear potentiometer, respectively. Displacement-type strain transducers (PI gages) were installed to record strain development at midspan. The behavior of the CFRP-concrete interface was monitored by strain gages. All test data were stored in a computerized data acquisition system.

4. TEST RESULTS

Experimental data are collected and interpreted to examine the performance of the embedded CFRP anchor systems. Material characteristics and element-level behavior are elaborated as well.

4.1 Ancillary Tests

4.1.1 Porosity of Polyester-silica

Figure 3(a) shows the water absorption of the polyester-silica and mortar matrices. For the mortar specimens, a steady increase was noted until 6 days; then, the absorption stabilized. The polyester-silica specimens exhibited constant responses, irrespective of immersion time. The apparent porosity of the mortar was also significantly higher than that of the polyester-silica (Figure 3(b)): an average increase of 208% at 14 days. The materials' capillary action was responsible for the kinetics of moisture flow (Hanzic et al. 2010). Overall, the polyester-silica composite was found to be unsusceptible to moisture ingress, which would benefit the durability of the proposed anchor system when used on site.

4.1.2 Strength of Polyester-silica

The time-dependent strength of the polyester-silica composite is plotted in Figure 4(a). The 12-hour strength was consistent at 24.5 MPa, on average, with a coefficient of variation of $COV = 0.018$, beyond which the degree of scatter went up and an average COV of 0.184 was recorded (1 day to 14 days). This may be attributable to the reactions between the polyester matrix and randomly spread silica particles when the chemical bond was set with liquid-solid attraction (Mohammed et al. 2018). The average strength converged after 7 days, which means that the aforementioned curing time of 14 days was sufficient to fully utilize the composite material in the present test program.

4.1.3 Bond Against Concrete

The average ultimate loads of the bond test specimens were 24.7 kN and 22.4 kN for the epoxy and polyester-silica matrices, respectively, as shown in Figure 4(b). All specimens failed by the middle block of the assembly (Figure 4(b), inset), rather than the bonded regions, which implies that the adhesion of the bonding agents was greater than the strength of the concrete. The bond capacities of the epoxy and polyester-silica against the concrete substrates were at least 2.5 MPa and 2.2 MPa, respectively, with the assumption that the applied load was equally distributed to the bonded areas of the three blocks. The polyester-silica matrix was, thus substantiated as a feasible material for the proposed embedded CFRP anchorage.

4.1.4 Behavior of Interface

Figure 5(a) provides the capacities of the interface specimens bonded with the polyester-silica composite. With an increase in the substrate angle, the capacities gradually rose. For instance, the average ultimate loads of the specimens at embedment angles of 10 and 25 degrees were 8.7 kN and 11.8 kN, respectively. The angle-dependent capacity of the epoxy-bonded interface, however, did not demonstrate such a trend (Figure 5(b)). These distinct interfacial responses can be explained by the failure mode of the specimens (Figure 5(c)). The polyester-silica-bonded specimens exhibited i) interface failure at angles of 10 and 15 degrees (Figure 5(c), left), accompanied by CFRP slippage along the bond-line, ii) fiber rupture at an angle of 25 degrees (Figure 5(c), middle), and iii) a mixture of these modes at 20 degrees. By contrast, regardless of substrate angle, the epoxy-bonded specimens consistently failed by fiber rupture (Figure 5(c), right).

4.2 Beam Tests

4.2.1 Load-carrying Capacity

Table 1 summarizes the load-carrying capacity of the test beams. The yield and ultimate loads of the unstrengthened beam (control) were 31.1 kN and 34.2 kN, respectively. An obvious relationship was noticed between the flexural capacity and CFRP-embedment angle in Phase I. The B100-25-PS beam (25 degrees) failed at a load of 58.1 kN, which was 11.5% higher than the B100-0-PS beam (0 degrees). The trend of the consistently increasing capacity with the embedment angle is graphed in Figure 6(a). Because the embedment angle of 25 degrees resulted in the most favorable capacity, it was adopted in Phases II and III.

The implications of local debonding, represented by the partially bonded CFRP sheets, were apparent (Figure 6(b)). The full-bond beam (100%) exhibited an increase of 69.9% in the ultimate load compared with the control beam. Unlike the variation of the yield load in the 80%- and 60%-bond beams, their ultimate loads were maintained. This fact illustrates that the occurrence of local debonding reduced the degree of stress-shearing between the internal and external reinforcements (steel and CFRP, respectively), thereby increasing the steel strains; however, the extent of CFRP-debonding was insufficient to influence the overall capacity of the beams (further discussions are available in the subsequent section). As the bond length decreased below 40%, noticeable capacity drops were recorded, which are ascribed to a dearth of the interaction between the beam and CFRP.

On the efficacy of epoxy-bonding in Phase III, the presence of the epoxy layer between the concrete substrate and the polyester-silica base precluded disintegration of the anchorage and induced an 8.8% increase in the ultimate load (B100-25-PSE vs. B100-25-PS in Table 1). Additional improvements in the capacity of the strengthened beams were accomplished by the mechanical fasteners: the failure loads of B100-25-PM and B100-25-PME were, respectively, 2.4% and 5.4% higher than that of B100-25-PSE.

4.2.2 Failure Mode

Pictured in Figure 7 are the failure modes of the selected beams in each test phase. The beam with plain CFRP-bonding (B100-0-PS) failed by end-peeling in conjunction with a diagonal tension crack connected to concrete crushing (Figure 7(a), left). When the embedded CFRP scheme was implemented in Phase I (Figure 7(a), middle and right), the failure plain shifted inside the anchorage and the contact between the polyester-silica and concrete disintegrated. Although the anchorage failure appeared analogous in all angles, the development of cracks adjacent to the embedded CFRP differed. Specifically, a localized crack path was observed in B100-10-PS (Figure 7(a), middle), while several secondary cracks were present in B100-25-PS (Figure 7(a), right). This observation signifies that internal stresses were better distributed in the higher-angled beam and, hence, its concrete section was efficiently used.

The bond-length-dependent failure of the strengthened beams with the substrate angle of 25 degrees is compared in Figure 7(b). Similar to B100-25-PS (Figure 7(a), right), B80-25-PS showed delamination with secondary cracks (Figure 7(b), left), meaning that the behavior of the embedded anchorage was preserved at a local debonding of 20% (80% bond length) near midspan. As the bond length decreased, the applied load was not properly transferred to the anchorage; consequently, regional damage dominated the failure of the beams (Figure 7(b), middle and right). In other words, the failure of these beams took place within the unbonded zone, away from the anchorage, owing to a lack of interaction between the concrete substrate and the strengthening system when the local debonding became more than 40% of the CFRP sheet (60% bond length or lower).

Figure 7(c) provides the failure of the Phase III beams. Even if the anchorage region of B100-25-PSE was impaired (Figure 7(c), left), no delamination was observed and the disintegration between the polyester-silica and concrete was not as significant as that of B100-25-PS (Figure 7(a), right). The mechanical fasteners retained the integrity of the anchorage (Figure 7(c), middle and right) until the beams failed. The secondary cracks in these beams reaffirmed the effective stress distributions by the PSE, PM, and PME anchors.

4.2.3 Flexural Behavior

The load-displacement behavior of the beams is shown in Figure 8. The control beam exhibited typical flexural responses, accompanied by a yield plateau and concrete crushing (Figure 8(a)). On account of the stress-sharing mechanism between the steel reinforcement and CFRP, B100-0-PS (0 degrees) revealed hardening after a yield load of 43.2 kN and abruptly failed. Such a tendency was also noted in the beams strengthened with the embedded CFRP sheets (Figures 8(a) and (b)), and there were marginal differences in the behavior of the beams, irrespective of substrate angle. As far as local debonding is concerned in Phase II (Figures 8(c) and (d)), the pre-peak behavior of B100-25-PS was alike to that of the beams with partial CFRP-bonding (0% to 80%), whereas the latter showed more displacements with low ultimate loads. It is speculated that the interfacial stresses between the concrete and CFRP dissipated through the unbonded area and were progressively transferred along the bond-line. The fluctuated loads in the post-peak behavior of the Phase II beams are attributed to the above-discussed regional damage, which occurred within the unbonded zone. As compared in Figure 8(e), the responses of the Phase III beams were akin to each other until B-100-25-PSE failed at a load of 63.2 kN. The combination of the mechanical fasteners and epoxy layers in the anchorage (B100-25-PME) impeded the brittle failure of the strengthened beam. An overall comparison among the test phases is given in Figure 8(f). The embedded CFRP system brought about betterment even with the 20% partial debonding (80% bonding, B80-25-PS).

The sectional rotation of the beams, obtained from the compression and tension strains at midspan, is provided in Figure 9 where the selected beams are shown for clarity. Even though the magnitudes of the rotation in the Phase I beams were minute at the order of 10^{-5} radians (Figure 9(a)), the embedment angle certainly affected the bending of the strengthened beams: the higher the angle, the less the rotation at midspan. The reason is that the horizontal deformation of CFRP was restrained as the angle increased. The sectional rotation of the B0-25-PS (0% bond) beam was almost identical to the rotation of the control beam (Figure 9(b)); however, the increased bond length led to a reduction in the rotation. Given the similarity among the B100-25-PS (Figure 9(a)) and B100-25-PM and -PME (Figure 9(c)) beams, the installation of the mechanical fasteners did not seem to be influential on the sectional rotation at midspan. The large rotation of B100-25-PSE in Figure 9(c), despite the embedment angle of 25 degrees, appears to be induced by the slip of the tensile PI gage.

4.2.4 Energy Dissipation

The flexural energy of the individual beams was determined by numerically integrating the load-displacement curves up to their initial peak loads, as summarized in Figure 10. The energy of the Phase I beams remained unchanged from 0 to 15 degrees and, then steadily increased with the angle (Figure 10(a)). The enhanced stress distribution near the anchorage, which was elaborated in the failure mode section, contributed to incrementally changing the energy. The detrimental ramifications of local CFRP-debonding are embodied in Figure 10(b). The energy consistently decreased with the bond length and leveled off beyond 20%. The mechanical fasteners and supplementary epoxy enabled higher energy dissipation in Phase III (Figure 10(c)), particularly for B100-25-PME, which showed an over 450% improvement relative to the case of the control beam.

4.2.5 Ductility Assessment

To quantify the flexural behavior of the beams, the concept of ductility was employed. Conforming to published literature (Spadea et al. 2001; Le et al. 2018), ductility indices (DI) were calculated using Equations 3 and 4

$$DI_{Disp} = \frac{\Delta_u}{\Delta_y} \quad (3)$$

$$DI_{Ener} = \frac{E_u}{E_y} \quad (4)$$

where DI_{Disp} and DI_{Ener} represent the displacement- and energy-based ductility of the beam, respectively; Δ_u and Δ_y are the displacements at the beam's yield and ultimate loads, respectively; and E_u and E_y are the energy values dissipated until the ultimate and yield loads of the beam, respectively.

The displacement and energy ductility indices of the Phase I beams decreased at an angle of greater than 15 degrees, as shown in Figure 11(a), primarily due to the upgraded yield loads and corresponding displacements (that is, the increased elastic portion in the full load history of the strengthened beams). With the decreased bond length in Phase II (Figure 11(b)), the ductility of the beams increased, except for the 20% and 0% cases that exhibited relatively close displacements between the yield and the initial peak loads. This ductility alteration mechanism, depending upon bond length, aligns with that of prestressed concrete beams with unbonded tendons concerning local slip (Naaman and Jeong 1995; Lee et al. 2015; Harmanci et al. 2016). When the mechanical anchorage and epoxy layers were used in Phase III (Figure 11(c)), the ductility of the beams substantially increased. For example, the energy ductility index of B100-25-PME (Figure 11(c)) was 96.7% higher than the index of B100-25-PS (Figure 11(a)).

Figures 11(d) to (f) appraise the ductility indices of the strengthened beams against that of the unstrengthened beam. The normalized ductility of the Phase I beams varied from 0.67 to 1.14, dependent upon embedment angle (Figure 11(d)), which is typical as stated in ACI 440.2R-17 (ACI 2017): the ductility of a reinforced concrete beam is generally reduced after CFRP-strengthening. From a design perspective, insufficient ductility can be addressed by adjusting strength reduction factors ($\phi = 0.65$ to 0.90) associated with steel strains at failure (ACI 2017). Because of the above-mentioned interfacial slip alongside relieved CFRP strains, the level of local debonding markedly changed the normalized ductility (Figure 11(e)). As evidenced by Figure 11(f), the ductility indices of the B100-25-PM beam were comparable to those of the control beam. Note that the normalized energy ductility of the Phase III beams was greater than their displacement counterpart, which was different from the trend shown in Figure 11(c), owing to the difference between $DI_{Ener} = 2.44$ and $DI_{Disp} = 1.64$ in the control beam.

4.2.6 CFRP Strain

The development of CFRP strains along the beam span is presented in Figure 12. The strengthened beam without an embedment angle (B100-0-PS, Figure 12(a)) exhibited archetypal responses, in that the strain patterns conformed to the envelope of the applied bending moment along the span. The midspan strain (SG3) was 6.81×10^{-3} and the strain outside the constant moment zone was 2.28×10^{-3} (average of SG2 and SG4). The strains of SG1 and SG5 near the CFRP-termination were negligible, although some fluctuation was logged because of the end-peeling in tandem with shear-cracking (Figure 7(a), left). The midspan strains of the beams with and without embedment angles are compared in Figure 12(b). As in the case of the sectional rotation (Figure 9(a)), stiffer strains were attained in B100-10-PS and B100-25-PS, corroborating the fact that the deformation of CFRP was related to the anchoring method. The bond length of CFRP was also influential on the strains within the shear-span of the beams (Figure 12(c)). The inconsistent propensity for the strains in Phase II can be explained by the irregular transfer of interfacial stresses along the bond-line where the bonded and unbonded regions were mixed. The strains of the Phase III beams near the anchorage (SG2, Figure 12(d)) developed precipitously and their magnitudes were smaller than those of the plain-bond beam (SG2 in Figure 12(a)). The midspan strains of the Phase III beams were generally similar, as shown in the inset of Figure 12(d).

The strain profile of CFRP at incremental load steps is depicted in Figure 13. The B100-0-PS and B100-10-PS beams demonstrated symmetrical responses at all load levels (Figures 13(a) and (b)), implying that the CFRP sheets were uniformly bonded. Conversely, the partially bonded beams such as B60-25-PS (Figure 13(c)) revealed asymmetric profiles since the interfacial stresses were not evenly transferred toward both ends of CFRP: one side attracted more stresses than the other when the regional damage took place (Figure 7(b)). The service load level responses of the respective beams were evaluated in Figures 13(d) to (f), at 60% of the B100-0-PS beam's capacity. There was insignificant dissimilarity among the fully bonded beams at variable embedment angles, and their service-level strains were below the maximum strain of the plain-bond beam ($\epsilon = 0.0017$, Figure 13(d)), which was lower than the debonding strain of $\epsilon_{fd} = 0.002$ per ACI 440.2R-17 (ACI 2017). Because of the erratic stress transfer explained above, the strain distributions of the partially bonded beams were complex (Figure 13(e)); nonetheless all strain levels were below the maximum strain of B100-0-PS. The strains of the Phase III beams on one side were distinct from the strains on the other side in which failure occurred (Figure 13(f)).

5. RESPONSE CHARACTERIZATION

Test data are analyzed to characterize the flexural capacities of CFRP-strengthened beams with embedment angles and partial bonding. Specific response patterns are identified and descriptive information is entailed.

5.1 Correlation

The joint variability between the test parameters and load-carrying capacities of the beams was measured by covariance. For comparison, the correlation between these variables, the normalized form of the covariance as defined in Equations 5 and 6 (Montgomery and Runger 2003), was employed.

$$\rho_{xy} = \frac{\text{cov}(x, y)}{\sqrt{V(x)V(y)}} \quad (5)$$

$$\text{cov}(x, y) = E(xy) - E(x)E(y) \quad (6)$$

where ρ_{xy} is the correlation coefficient of variables x and y ; $\text{cov}(x, y)$ are the covariance of the variables; and $V(\cdot)$ and $E(\cdot)$ are the variance and the expected value of each variable, respectively. In accordance with the calculated correlation coefficients (Figure 14(a)), the yield and ultimate loads of the beams were significantly correlated with the strengthening configurations (that is, ρ_{xy} is close to unity). The correlation coefficients for the yield load belonging to the embedment angle and bond length categories were 0.985 and 0.988, respectively. The coefficient for the ultimate load related to the embedment angle was 0.902, which was lower than the corresponding coefficient associated with the bond length, 0.975. It is, thus, stated that the ultimate capacity of the beams was more susceptible to the local CFRP-debonding in comparison with the embedment angle.

5.2 Sensitivity

The dependency of the flexural capacities on the strengthening schemes was assessed by modifying the classical concept of relative sensitivity (Brylinsky 1972). Equation 7 delineates the proposed global sensitivity coefficient, s , of the test beams

$$s = \left\langle \frac{\Delta y}{\Delta x} \left(\frac{x_0}{y(x_0)} \right) \right\rangle \quad (7)$$

where $\langle \cdot \rangle$ indicates the average of the local sensitivity values for variables x and y ; $\Delta x = x_j - x_i$ with $j > i$; $\Delta y = y_j - y_i$ with the condition same to Δx ; and x_0 and $y(x_0)$ are the reference values of the independent variable (embedment angle of 25 degrees or bond length of 100%) and its dependent variable (yield or ultimate load of the beam), respectively. Shown in Figure 14(b) are the sensitivity coefficients of the strengthened beams. The coefficients for the yield and ultimate loads against the embedment angle were 0.144 and 0.139, respectively. When the bond length was of interest, a considerable increase in the sensitivity was calculated to be 0.349 and 0.421 for the yield and ultimate loads, respectively. These observations clarify the practical significance of the variable embedment angle and bond length on altering the load-carrying capacity of the strengthened beams.

6. SUMMARY AND CONCLUSIONS

This report has dealt with a novel anchor system for CFRP-strengthened beams in order to address the unfavorable consequences of end-peeling. The proposed system was composed of angled CFRP sheets embedded in the anchorage, which were overlaid and covered by a durable polyester-silica composite. Multi-phase tests were conducted to investigate the material, interfacial, and flexural responses of the element- and structure-level specimens. Analytical approaches (correlation and sensitivity) characterized the effects of CFRP embedment angles and local debonding on the capacity of the strengthened beams. The following conclusions are drawn:

- The water absorption and apparent porosity of the polyester-silica composite were remarkably lower than those of ordinary mortar, justifying the use of the former in the proposed anchor system from a durability standpoint. After 7 days of casting, the average compressive strength of the polyester-silica remained over 37.5 MPa (5,400 psi).
- The polyester-silica matrix revealed favorable bond to concrete with an average adhesion capacity of at least 2.2 MPa (320 psi). The ascending angle of the polyester-silica substrate in the embedded anchors increased the interfacial capacity by altering failure modes from contact disintegration to fiber rupture.
- The flexural capacity of the strengthened beams increased as the embedment angle went up, while the capacity decreased with local CFRP-debonding, especially below 40% of the full bond (60% debonding). The epoxy layers inside the anchorage intensified the grooved CFRP system together with the mechanical fasteners, which also led to the ductile behavior of the beam.
- Compared with the fully bonded beams (100% bond), the partially bonded beams (60% to 20% bond) demonstrated regional failure due to the improper interaction between the concrete substrate and CFRP outside the anchorage zone.
- The energy dissipation and ductility of the strengthened beams varied with the embedment angle and bond length. The anchoring methods altered the deformation of CFRP. Partial bonding was responsible for the irregular stress transfer along the bond line, where the bonded and unbonded regions coexisted, and for the interfacial slip relieving CFRP strains.
- The correlation coefficients indicated that the local debonding was more influential on and sensitive to the load-carrying capacity of the strengthened beams than the embedment angle.

7. REFERENCES

- ACI. 2007. Report on fiber-reinforced polymer (FRP) reinforcement for concrete structures (ACI 440.R-07), American Concrete Institute, Farmington Hills, MI.
- ACI. 2017. Guide for the design and construction of externally bonded FRP systems for strengthening concrete structures (ACI 440.2R-17), American Concrete Institute, Farmington Hills, MI.
- ASTM. 2009. Standard test method for dry and wet bulk density, water absorption, and apparent porosity of thin sections of glass-fiber reinforced concrete (C948), ASTM International, West Conshohocken, PA.
- ASTM. 2015. Standard test method for compressive strength of cylindrical concrete specimens (C39), ASTM International, West Conshohocken, PA.
- Brylinsky, M. 1972. Systems analysis and simulation in ecology, 81-101, Academic, New York, NY.
- CSA. 2014. Canadian highway bridge design code (CAN/CSA-S6-14), CSA International, Toronto, ON, Canada.
- Hanzic, L., Kosec, L., and Anzel, I. 2010. Capillary absorption in concrete and the Lucas-Washburn equation, *Cement & Concrete Composites*, 32, 84-91.
- Harmanci, Y.E., Michels, J., Czaderski, C., and Motavalli, M. 2016. Calculation technique for externally unbonded CFRP strips in structural concrete retrofitting, *Journal of Engineering Mechanics*, 142(6), 04016026.
- Hollaway, L.C. 2010. A review of the present and future utilisation of FRP composites in the civil infrastructure with reference to their important in-service properties, *Construction and Building Materials*, 24, 2419-2445.
- Kalfat, R., Al-Mahaidi, R., and Smith, S.T. 2013. Anchorage devices used to improve the performance of reinforced concrete beams retrofitted with FRP composites: state-of-the-art review, *Journal of Composites for Construction*, 17(1), 14-33.
- Le, T.D., Pham, T.M., Hao, H., and Hao, Y. 2018. Flexural behaviour of precast segmental concrete beams internally prestressed with unbonded CFRP tendons under four-point loading, *Engineering Structures*, 168, 371-383.
- Lee, C., Shin, S., and Lee, S. 2015. Modelling of load-deflection of concrete beams internally prestressed with unbonded CFRP tendons, *Magazine of Concrete Research*, 67(13), 730-746.
- Lee, J. and Lopez, M.M. 2019. Frictional bond-slip model for the concrete-FRP interface under the FRP U-wrap region, *Construction and Building Materials*, 194, 226-237.
- Mohammed, M., Parry, T., Thom, N., and Grenfell, J. 2018. Investigation into the bond strength of bitumen-fibre mastic, *Construction and Building Materials*, 190, 382-391.
- Montgomery, D.C. and Runger, G.C. 2003. Applied statistics and probability for engineers, Wiley, New York, NY.

Naaman, A.E. and Jeong, S.M. 1995. Structural ductility of concrete beams prestressed with FRP tendons, Proceedings of the 2nd International RILEM Symposium on Non-metallic (FRP) Reinforcement for Concrete Structures, E & FN Spon, London, UK, 379-386.

Pan, Y., Shi, J., and Xian, G. 2019. Experimental and numerical study of the CFRP-to-concrete bonded joints after water immersion, Composite Structures, 218, 95-106.

Spadea, G., Swamy, R.N., and Bencardino, F. 2001. Strength and ductility of RC beams repaired with bonded CFRP laminates, Journal of Bridge Engineering, 6(5), 349-355.

Smith, S.T. and Teng, J.G. 2002. FRP-strengthened RC beams I: review of debonding strength models, Engineering Structures, 24, 385-395.

Wan, B., Jiang, C., and Wu, Y.-F. 2018. Effect of defects in externally bonded FRP reinforced concrete, Construction and Building Materials, 172, 63-76.

Zhou, Y., Wang, X., Sui, L., Xinig, F., Huang, Z., Chen, C., Li, P., and Mei, L. 2018. Effect of mechanical fastening pressure on the bond behaviors of hybrid-bonded FRP to concrete interface, Composite Structures, 204, 731-744.

Table 1. Test beams

Phase	Beam	CFRP-bond length	CFRP-embedment		Load (kN)	
			Angle	Configuration	Yield	Ultimate
I	Control	None	None	None	31.1	34.2
	B100-0-PS	100%	0°	PS	43.2	52.1
	B100-10-PS	100%	10°	PS	46.0	52.9
	B100-15-PS	100%	15°	PS	48.5	53.3
	B100-20-PS	100%	20°	PS	49.9	55.5
	B100-25-PS	100%	25°	PS	50.4	58.1
II	B80-25-PS	80%	25°	PS	47.3	54.6
	B60-25-PS	60%	25°	PS	42.3	54.0
	B40-25-PS	40%	25°	PS	37.5	48.4
	B20-25-PS	20%	25°	PS	36.6	43.5
	B0-25-PS	0%	25°	PS	32.8	36.9
III	B100-25-PSE	100%	25°	PS+EP	55.4	63.2
	B100-25-PM	100%	25°	PS+MF	56.7	64.7
	B100-25-PME	100%	25°	PS+MF+EP	59.4	66.6

PS = polyester-silica; MF = mechanical fastener; EP = epoxy

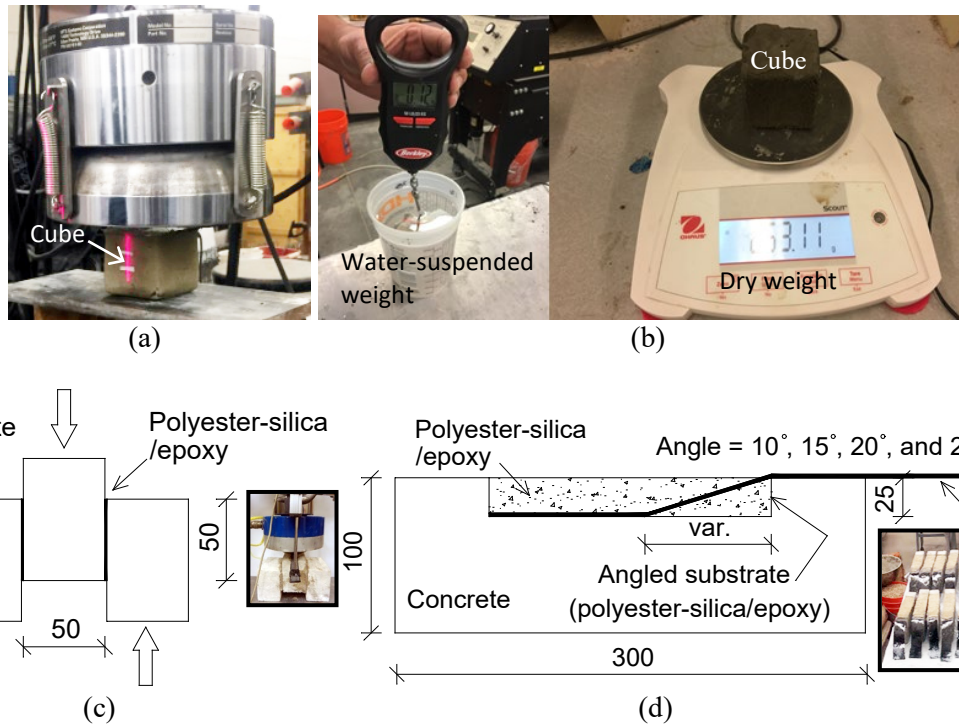


Figure 1. Ancillary tests: (a) polyester-silica cube; (b) porosity; (c) bond; (d) interface

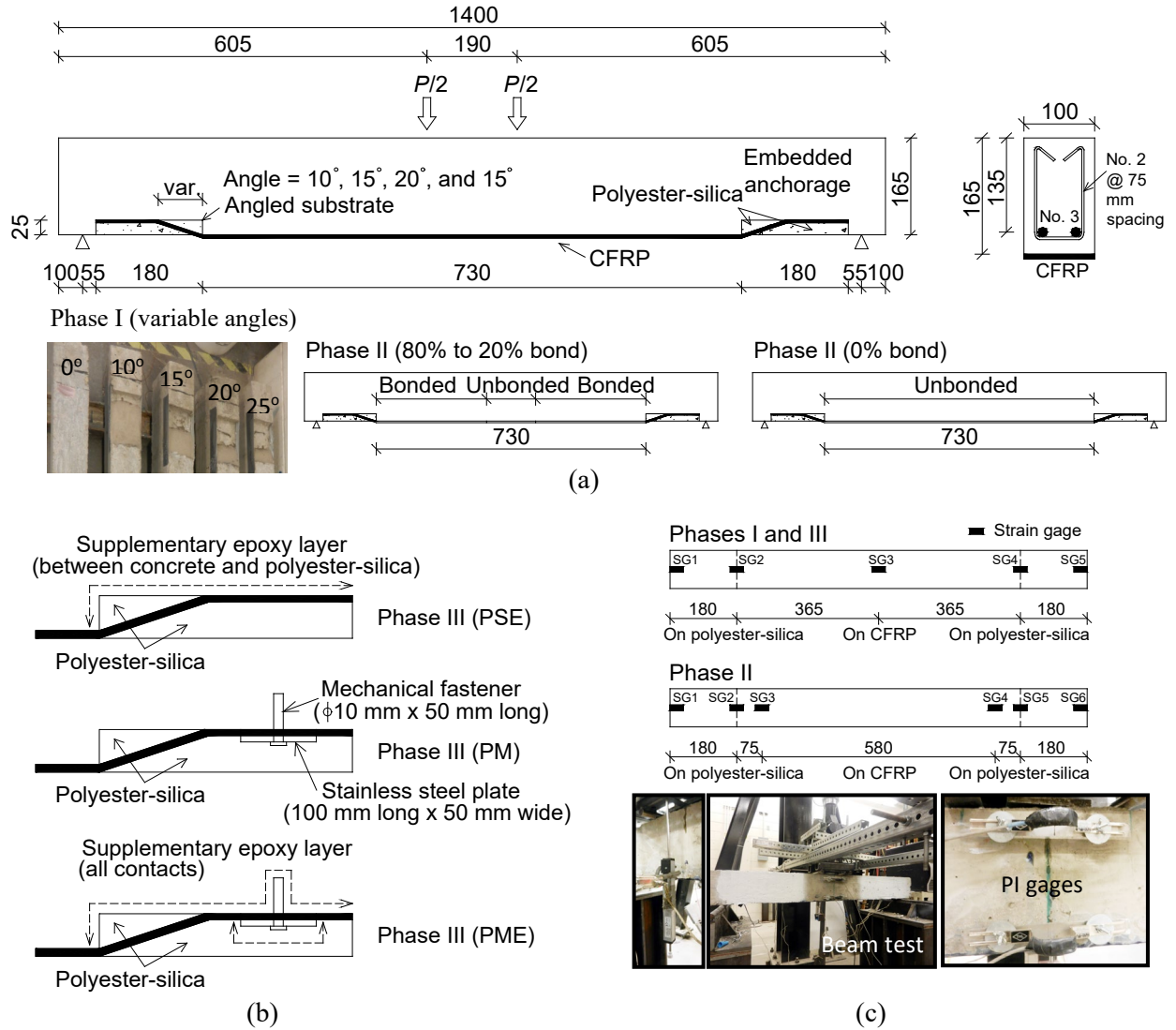


Figure 2. Beam details: (a) dimension and strengthening scheme; (b) anchorage of Phase III; (c) test setup and instrumentation

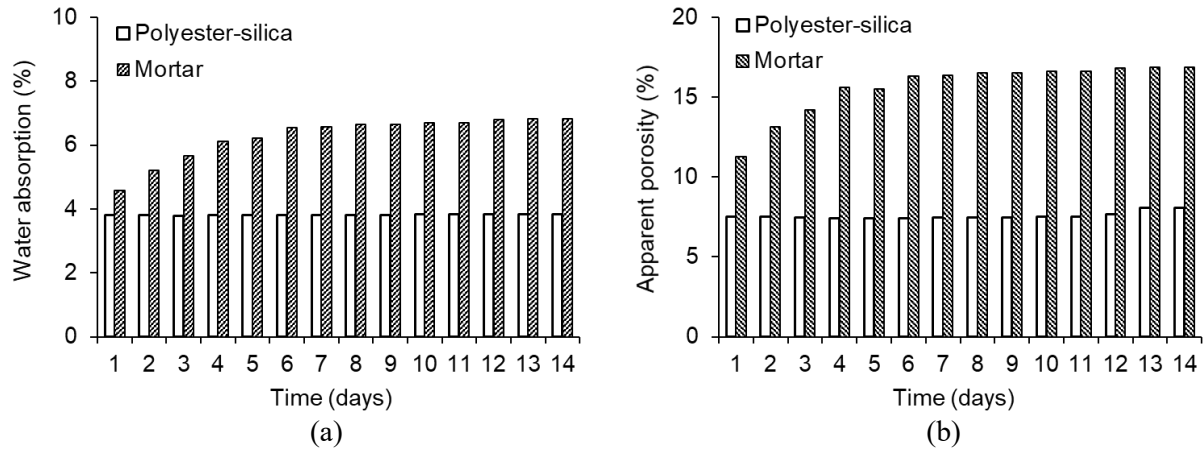


Figure 3. Porosity test: (a) average water absorption; (b) average apparent porosity

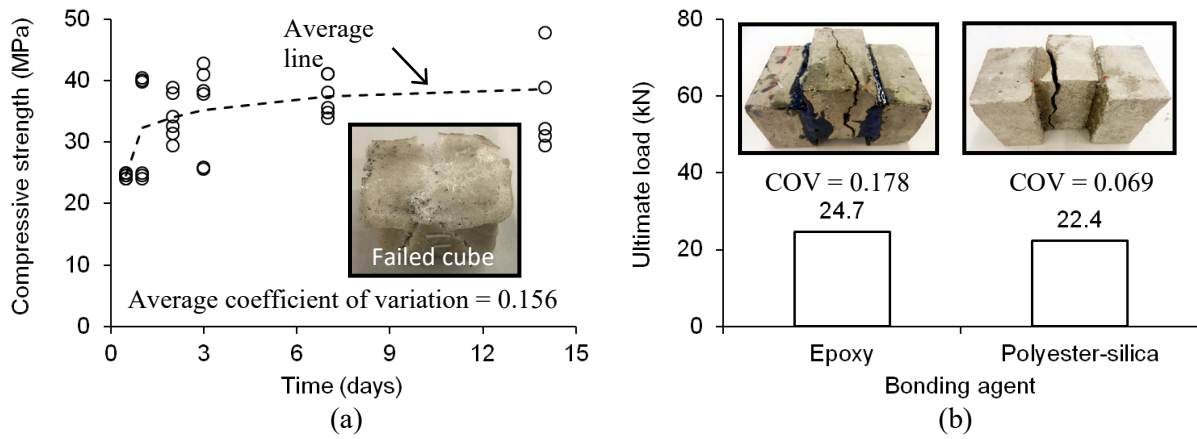


Figure 4. Material test: (a) polyester-silica in compression; (b) bond with concrete substrate

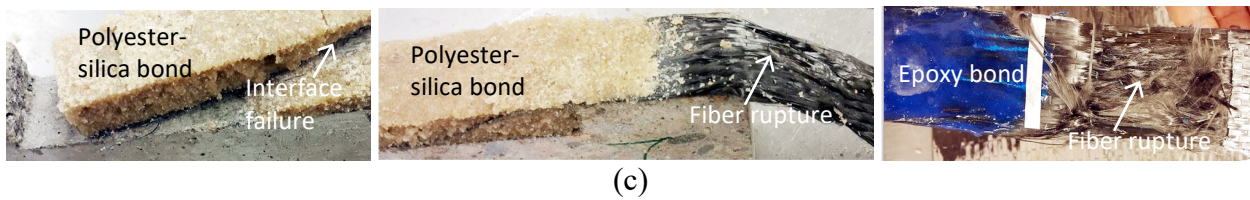
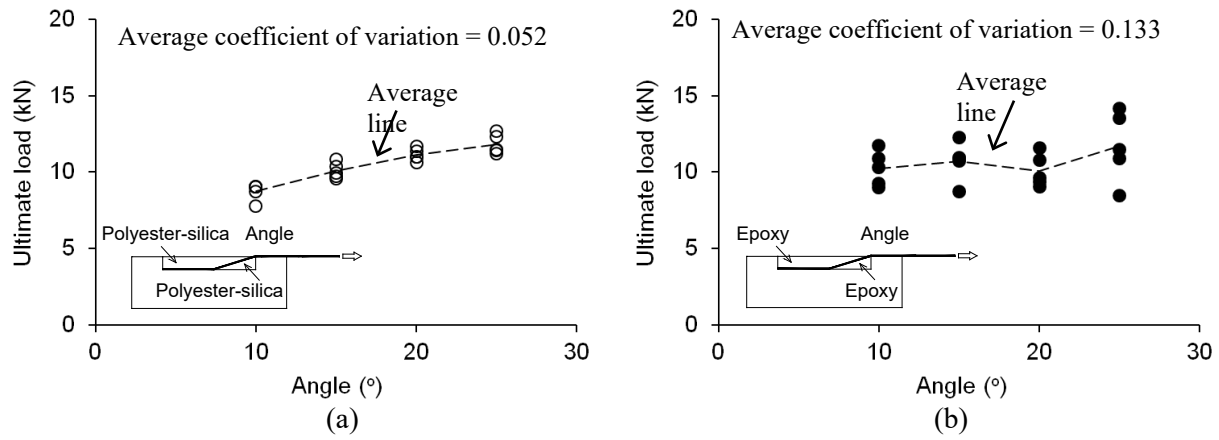


Figure 5. Interface test: (a) polyester-silica; (b) epoxy; (c) failure mode

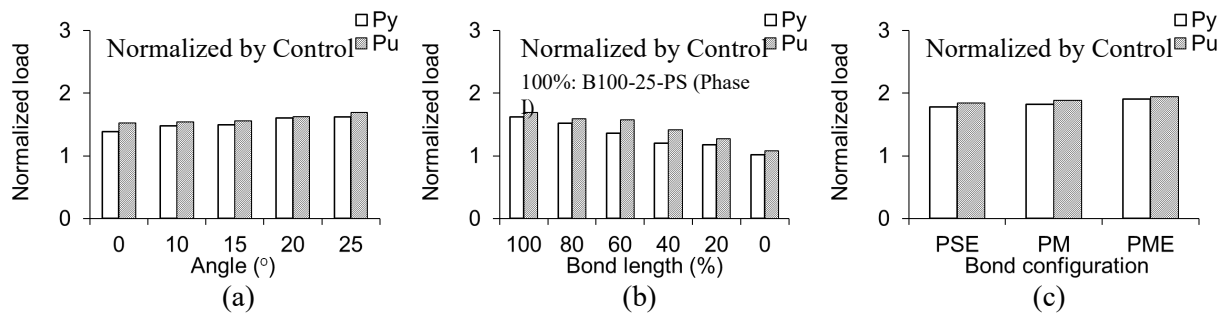


Figure 6. Comparison of flexural capacity: (a) Phase I; (b) Phase II; (c) Phase III

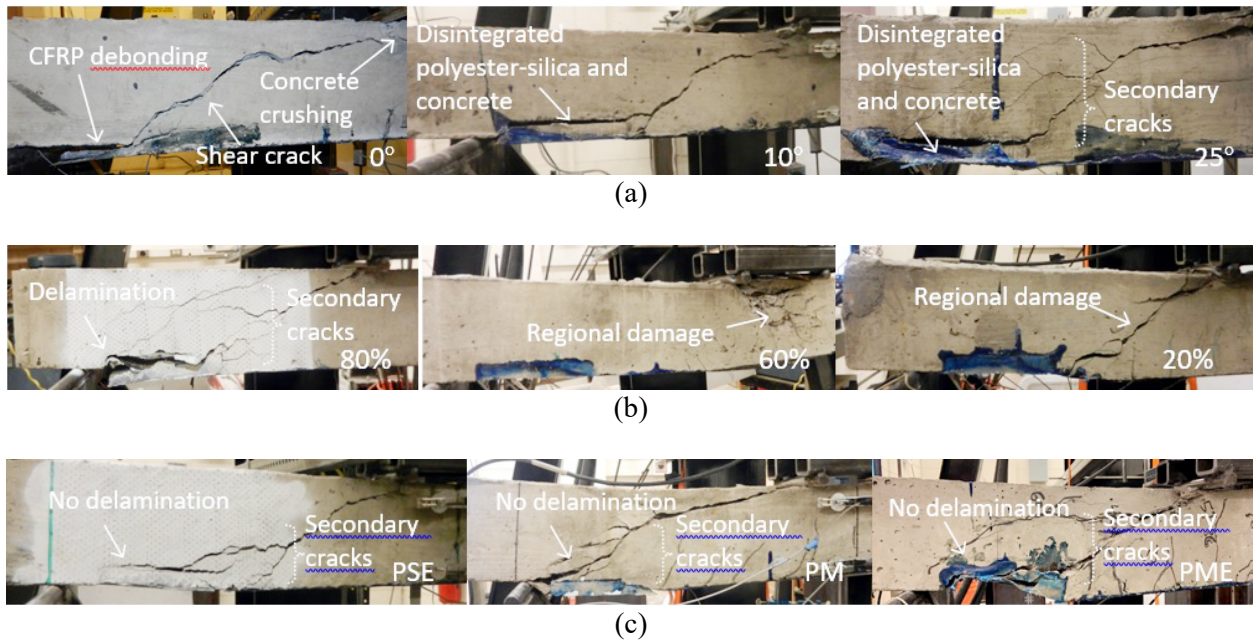


Figure 7. Failure mode: (a) Phase I; (b) Phase II; (c) Phase III

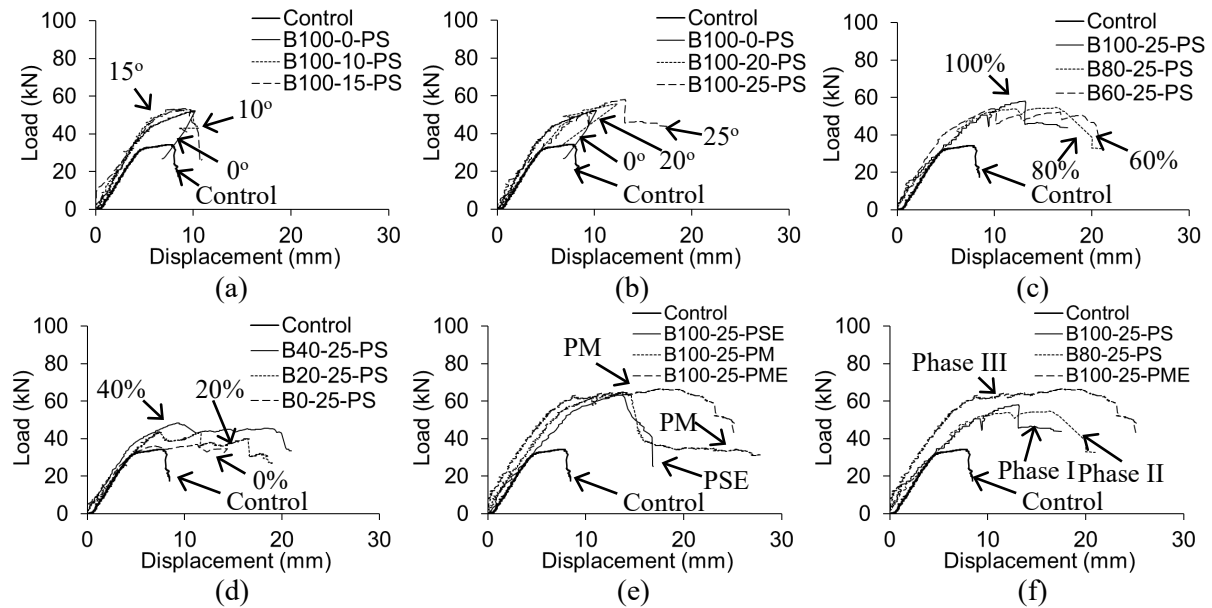


Figure 8. Load-displacement behavior: (a) Phase I (0°, 10°, and 15°); (b) Phase I (0°, 20°, and 25°); (c) Phase II (80% to 60% bond); (d) Phase II (40% to 0% bond); (e) Phase III; (f) comparison among phases

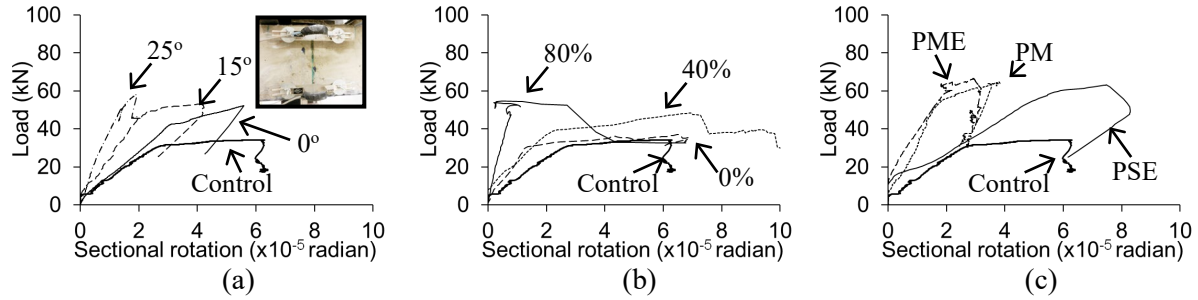


Figure 9. Sectional rotation at midspan: (a) Phase I; (b) Phase II; (c) Phase III

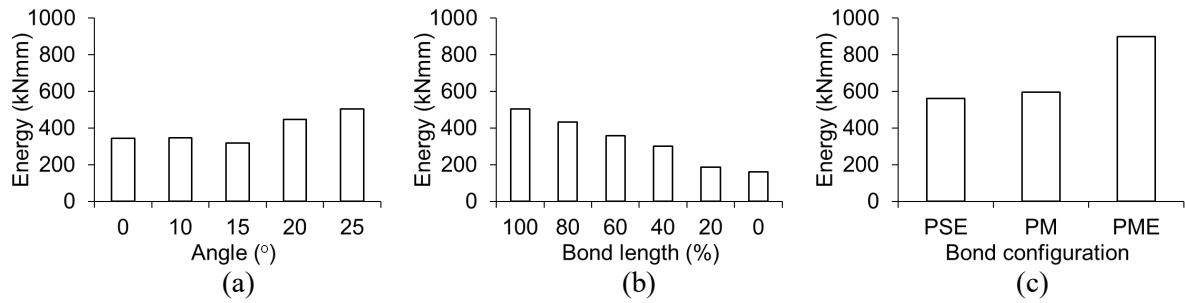


Figure 10. Flexural energy up to initial peak load: (a) Phase I; (b) Phase II; (c) Phase III

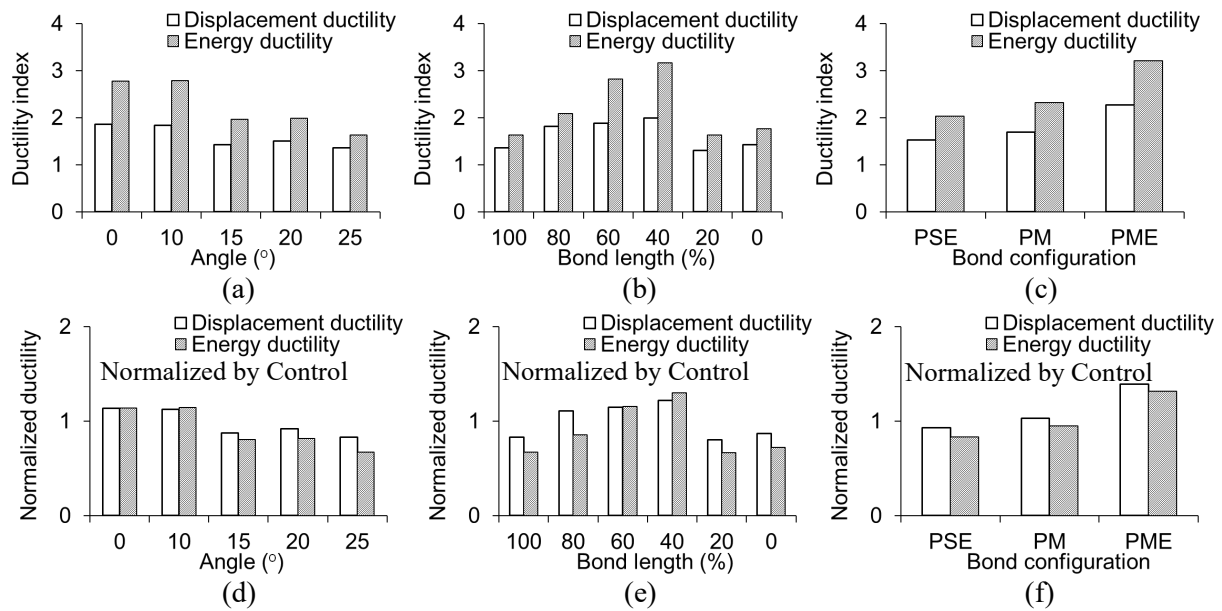


Figure 11. Ductility: (a) Phase I; (b) Phase II; (c) Phase III; (d) normalized Phase I; (e) normalized Phase II; (f) normalized Phase III

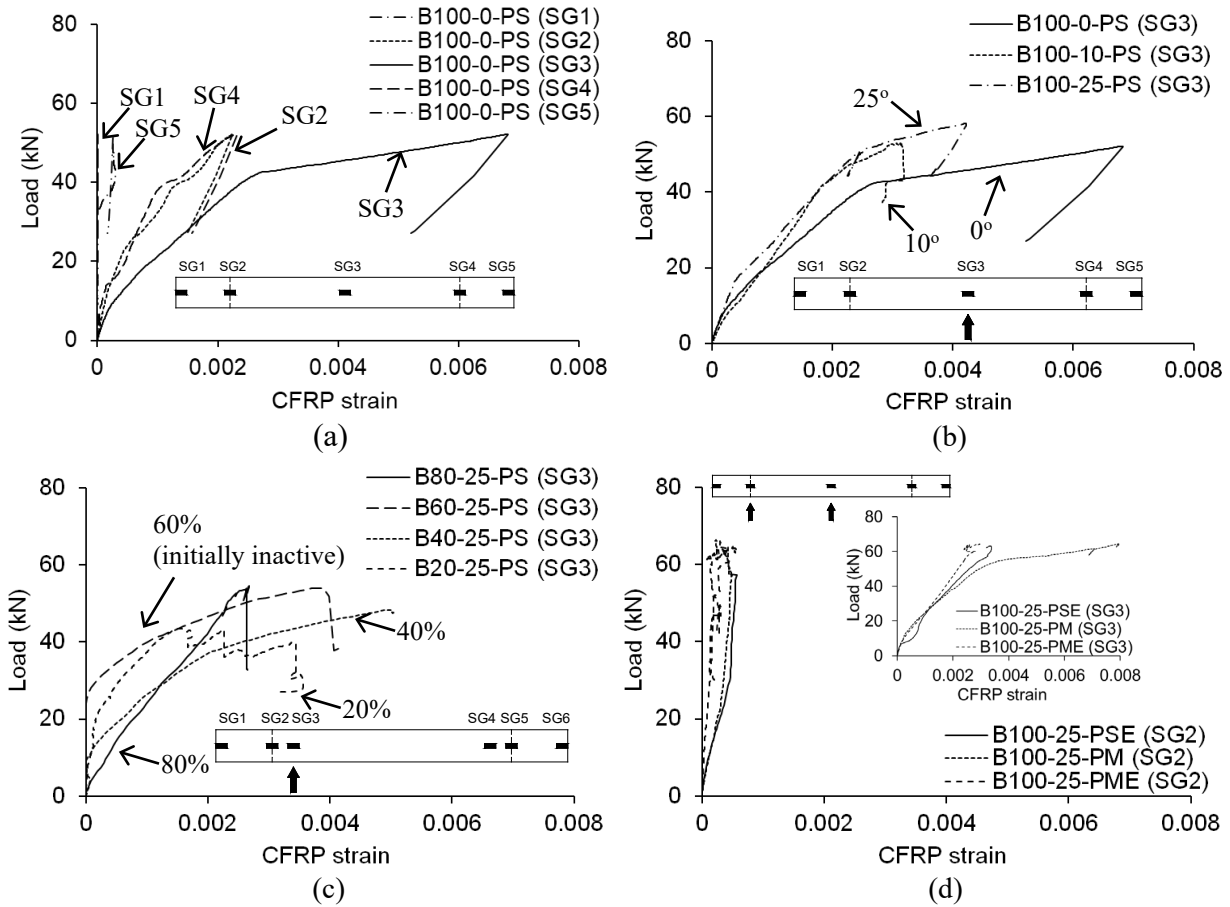


Figure 12. CFRP strain development: (a) plain CFRP bonding; (b) midspan strain at embedment angles; (c) comparison at strain gage; (d) comparison at strain gages 2 and 3

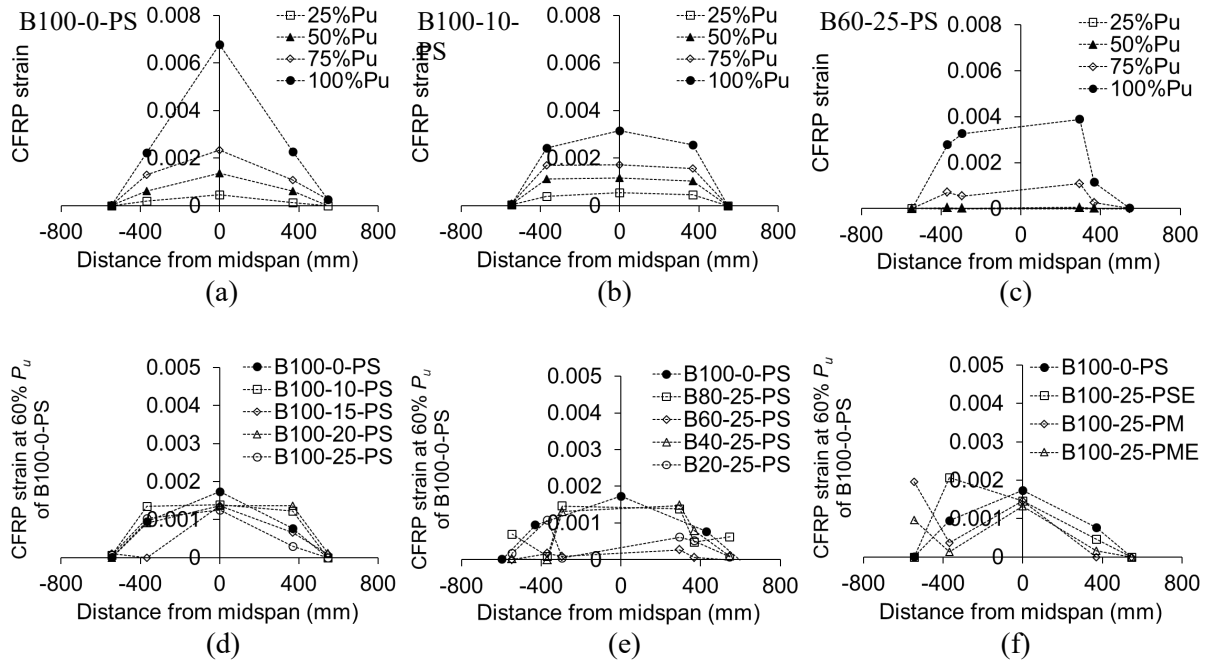


Figure 13. CFRP strain profile: (a) Phase I (0 degrees); (b) Phase I (10 degrees); (c) Phase II (60% bond); (c) Phase I (service); (d) Phase II (service); (e) Phase III (service)

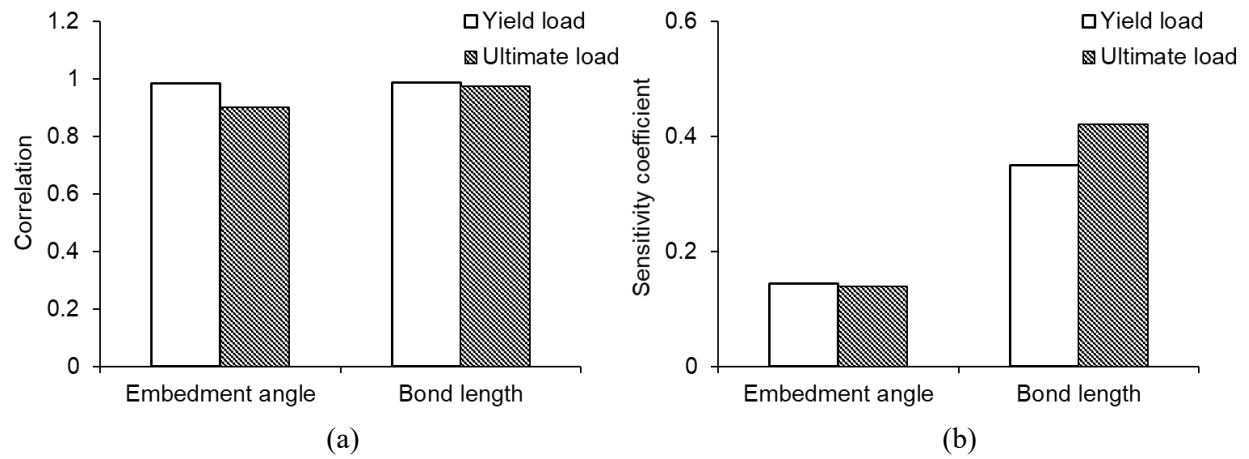


Figure 14. Characterized response: (a) correlation; (b) sensitivity